Science Advances
AAAS

advances.sciencemag.org/cgi/content/full/6/29/eabb2695/DC1

Supplementary Materials for

Integrated cascade nanozyme catalyzes in vivo ROS scavenging for anti-inflammatory therapy

Yufeng Liu, Yuan Cheng, He Zhang, Min Zhou, Yijun Yu, Shichao Lin, Bo Jiang, Xiaozhi Zhao, Leiying Miao, Chuan-Wan Wei, Quanyi Liu, Ying-Wu Lin, Yan Du, Christopher J. Butch*, Hui Wei*

*Corresponding author. Email: weihui@nju.edu.cn (H.W.); chrisbutch@gmail.com (C.J.B.)

Published 17 July 2020, *Sci. Adv.* **6**, eabb2695 (2020)
DOI: 10.1126/sciadv.abb2695

This PDF file includes:

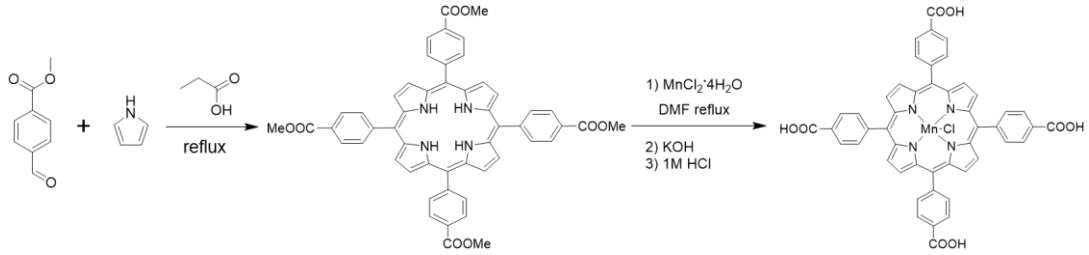

Scheme S1. Synthetic procedure of manganese porphyrin (TCPP-Mn).

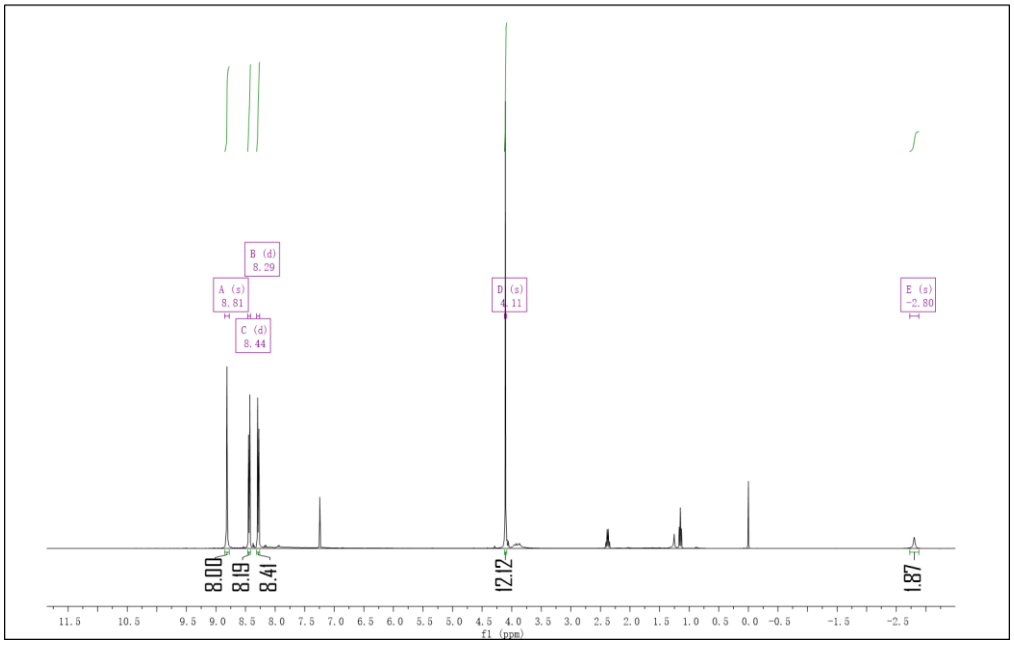

Figure S1. ^{1}H-NMR spectrum of TCPP-Mn.

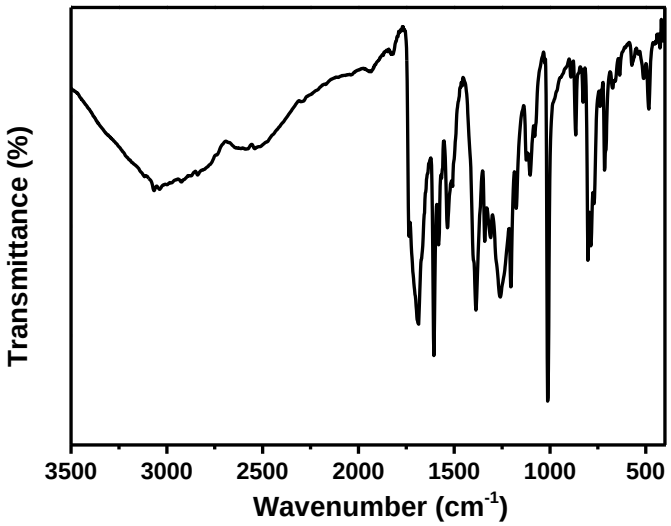

Figure S2. Fourier transform infrared spectrum of TCPP-Mn.

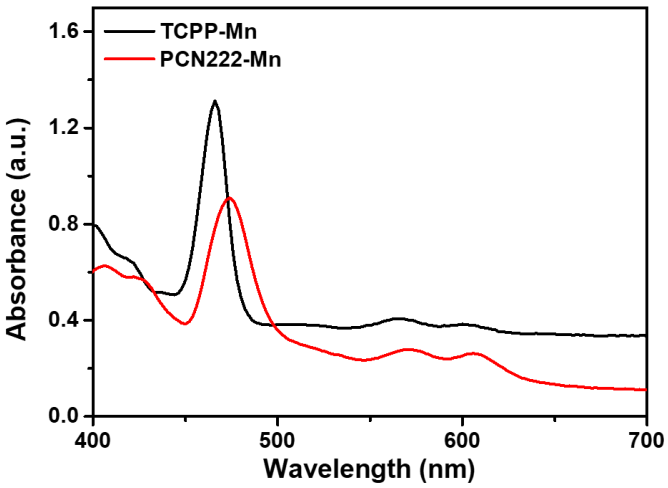

Figure S3. Absorption spectra of TCPP-Mn and PCN222-Mn.

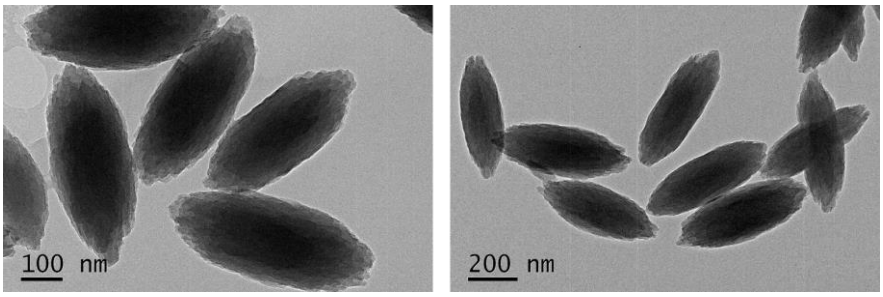

Figure S4. TEM images of PCN222-Mn.

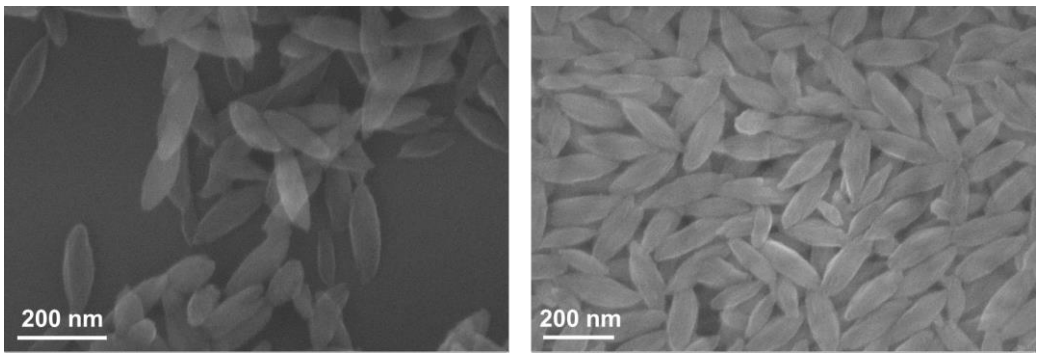

Figure S5. SEM images of PCN222-Mn.

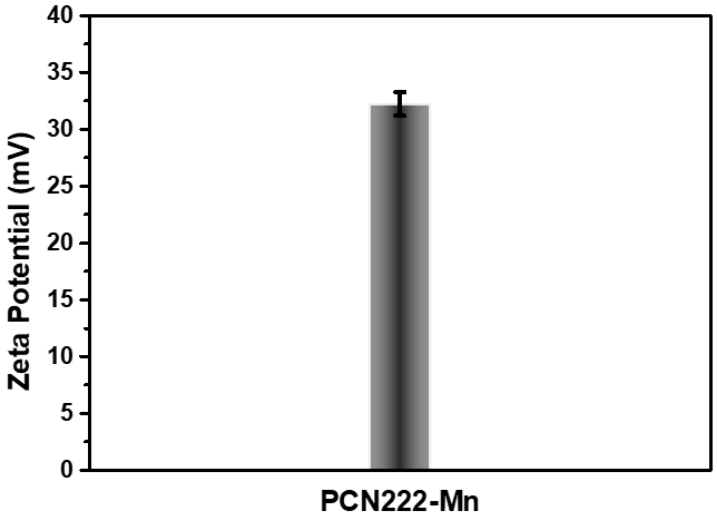

Figure S6. Zeta potential of PCN222-Mn.

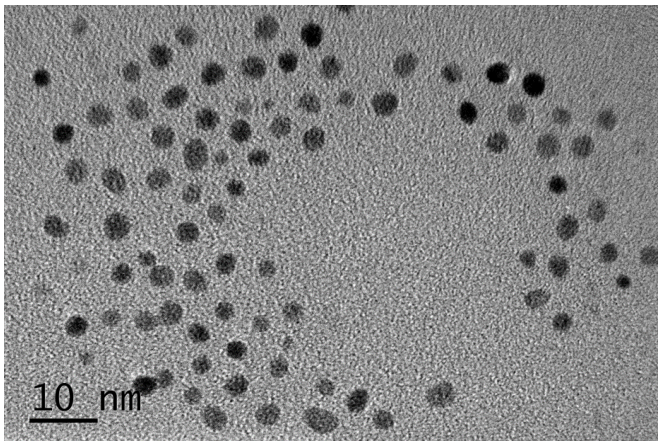

Figure S7. TEM image of Pt NPs.

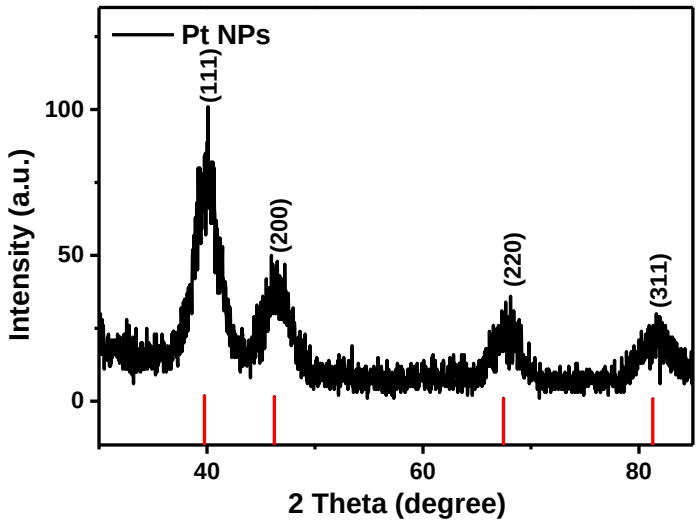

Figure S8. PXRD pattern of Pt NPs.

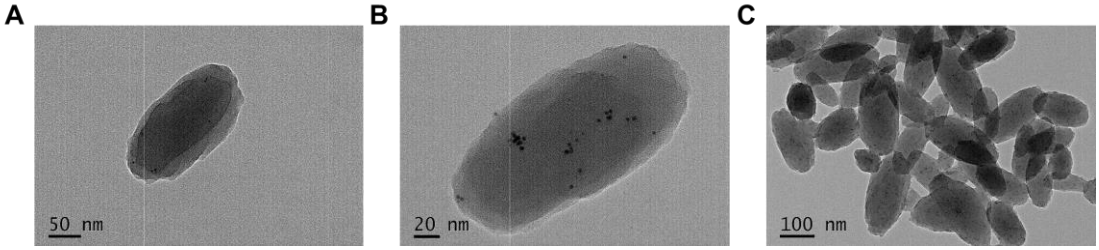

Figure S9. TEM images of (A) Pt@PCN222-Mn-1, (B) Pt@PCN222-Mn-3, and (C) Pt@PCN222-Mn-5.

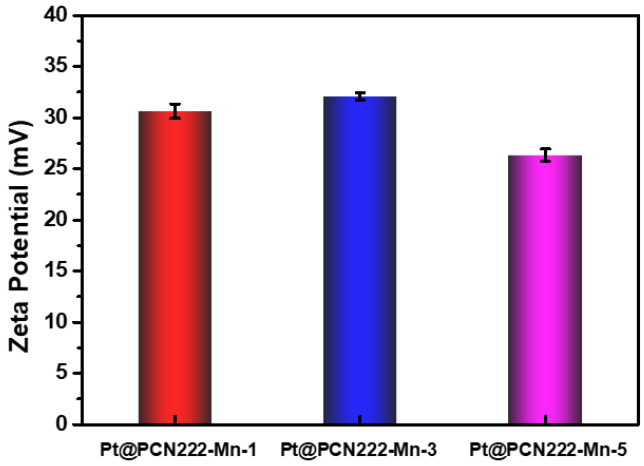

Figure S10. Zeta potentials of Pt@PCN222-Mn-1, Pt@PCN222-Mn-3, and Pt@PCN222-Mn-5.

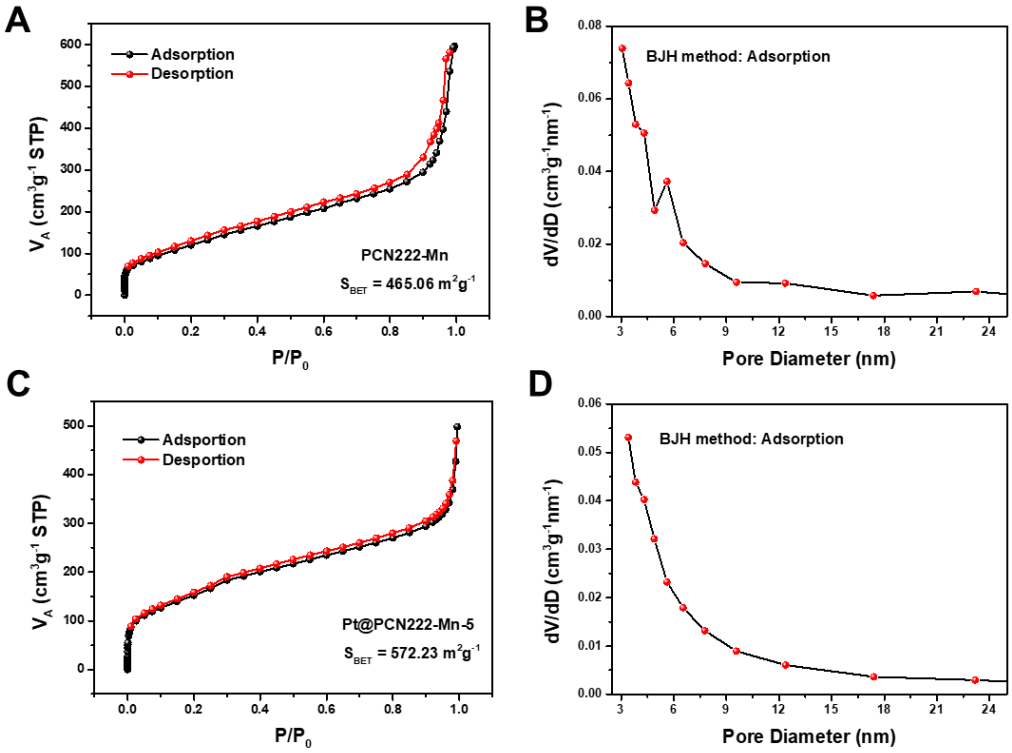

Figure S11. (A) N_2 adsorption-desorption isotherm and (B) pore size distribution curve of PCN222-Mn. (C) N_2 adsorption-desorption isotherm and (D) pore size distribution curve of Pt@PCN222-Mn-5.

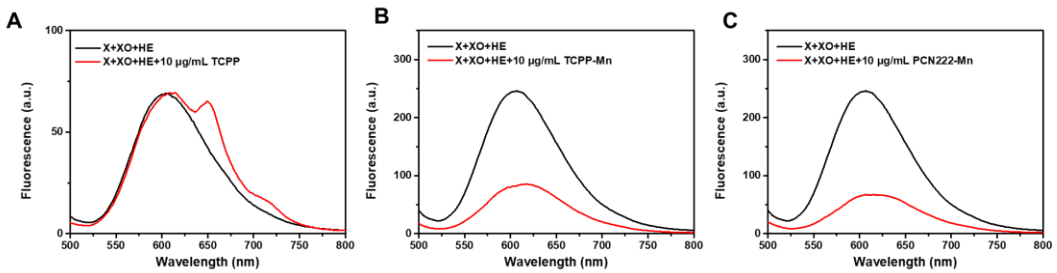

Figure S12. Fluorescent spectra of the mixture of xanthine (X), xanthine oxidase (XO), and hydroethidine (HE) in the absence and presence of (A) TCPP, (B) TCPP-Mn, and (C) PCN222-Mn.

The SOD-like activities of TCPP, TCPP-Mn, and PCN222-Mn were assessed by monitoring their capability to eliminate $^{\bullet}O_2^-$ generated from the mixture of xanthine (X) and xanthine oxidase (XO). Hydroethidine (HE), a $^{\bullet}O_2^-$ specific dye, was used to quantify the level of $^{\bullet}O_2^-$.

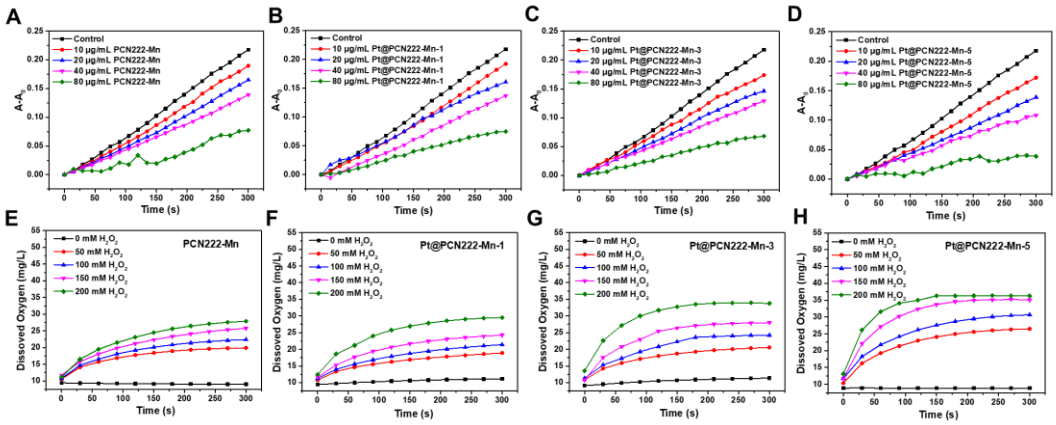

Figure S13. Kinetic curves of A-A_0 (550 nm) for monitoring the reduction of NBT with xanthine and xanthine oxidase in the absence and presence of different concentrations of (A) PCN222-Mn, (B) Pt@PCN222-Mn-1, (C) Pt@PCN222-Mn-3, and (D) Pt@PCN222-Mn-5, respectively. Kinetic curves of O_2 generation from the decomposition of H_2O_2 (0, 50, 100, 150, and 200 mM) in the presence of (E) PCN222-Mn, (F) Pt@PCN222-Mn-1, (G) Pt@PCN222-Mn-3, and (H) Pt@PCN222-Mn-5 (20 μg/mL), respectively.

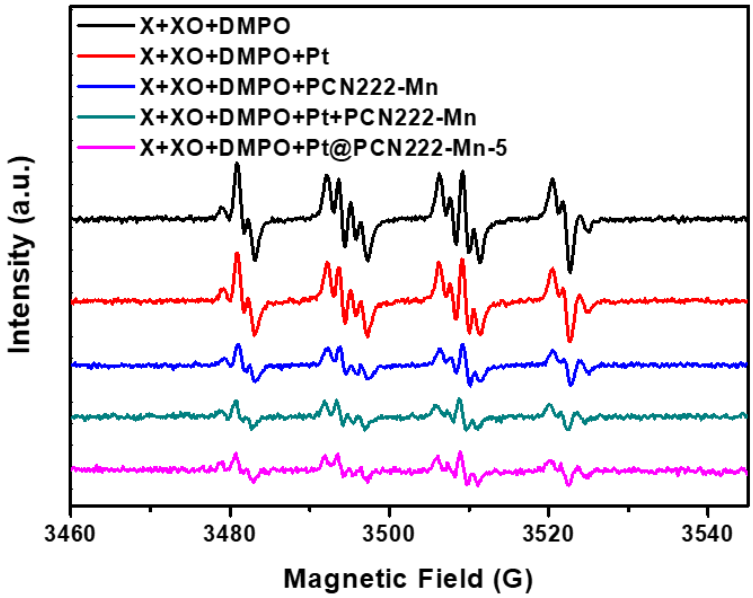

Figure S14. EPR spectra of the mixed solution of xanthine (X), xanthine oxidase (XO), and 5,5-dimethyl-1-pyrroline-N-oxide (DMPO) in the absence and presence of Pt, PCN222-Mn, Pt + PCN222-Mn, and Pt@PCN222-Mn-5.

As shown in Figure S14, 5,5-dimethyl-1-pyrroline-N-oxide (DMPO) was used to trap the $^{\bullet}O_2^-$, which was generated from the reaction of xanthine (X) with xanthine oxidase (XO). Since $^{\bullet}O_2^-$ is very active and unstable in aqueous solution, a major adduct of DMPO-$^{\bullet}$OOH was observed. The intensity of the EPR signals of DMPO-$^{\bullet}$OOH decreased upon addition of Pt, PCN222-Mn, Pt + PCN222-Mn, and Pt@PCN222-Mn-5. Moreover, among the four groups, Pt@PCN222-Mn-5 treatment produced the weakest signals, indicating the highest SOD-like activity of the integrated cascade nanozyme.

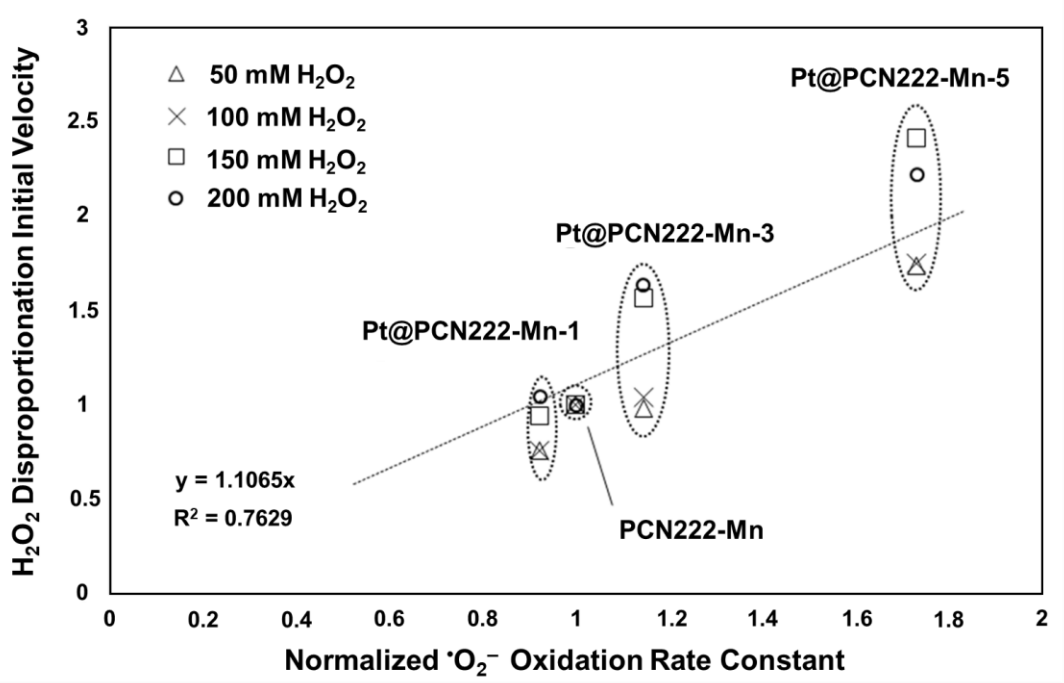

Figure S15. Kinetic Analysis of SOD/CAT Cascade. Correlogram between the observed rate of $^{\bullet}O_2^-$ oxidation and H_2O_2 disproportionation.

Generation of Fig S15: The data shown in Fig. S13A-13D were fit with the following simple first order kinetic model to derive an overall rate constant $k_{\cdot O_2 OxNP}$. Each nanoparticle formulation has its own $k_{\cdot O_2 OxNP}$.rate constant, and these are assumed to be constant throughout the experiments. With this in mind, for each kinetic run, the rate equation for superoxide concentration as a function of time is as follows.

$$\frac{d[\cdot O_2^-]}{dt} = Generation - [\cdot O_2^-] \cdot k_{\cdot O_2 OxDye} - [\cdot O_2^-] \cdot [NP] \cdot k_{\cdot O_2 OxNP}$$

Due to the lack of time course data on the concentration of $^{\bullet}O_2^-$, a pseudo-steady state approximation was employed by setting $\frac{d[\cdot O_2^-]}{dt} = 0$.

Under this approximation the rate of generation and consumption are assumed equal. From the runs without nanozyme, we can see that the rate of generation is constant between runs. The relative concentration of $^{\bullet}O_2^-$ can thus be inferred from the observed rate of NBT reduction. This is then used to infer the rate of nanoparticle catalyzed oxidation of $^{\bullet}O_2^-$. From this methodology the following relative rate constants were derived. As each nanoparticle was evaluated at four concentrations, the constants are reported as average ± the standard deviation, and normalized to PCN222-Mn. The results are PCN222-Mn (1.00 ± 0.23), Pt@PCN222-Mn-1 (0.92 ± 0.15), Pt@PCN222-Mn-3 (1.15 ± 0.17), and Pt@PCN222-Mn-5 (1.73 ± 0.57).

These rate constants were then compared to the initial velocities of H_2O_2 disproportionation, (once again normalized to PCN222-Mn at each H_2O_2 concentration), and good correlation was observed between the two reaction rates as shown above. The correlation of these two rates suggests that H_2O_2 disproportionation is rate limiting in

the overall reaction. This may be because H_2O_2 can interact with the Mn nucleus, thus occupying the active site, and blocking the interaction with a new $^{\bullet}O_2^-$ molecule. The larger the H_2O_2 concentration, the greater this effect. Consequently, by collocating the two reactive metal centers, the cascade nanozyme can remove the diffusion barrier and lower the overall H_2O_2 concentration, thus increasing the reactivity of the Mn center. The observed minimal synergistic effect of PCN222-Mn combined with platinum nanoparticles further supports this inference. In PCN222-Mn, the H_2O_2 is generated inside the nanoparticle and must diffuse outward. The reduction in concentration of outside the nanoparticle by Pt NPs, will only slightly accelerate this step as compared to lowering the concentration within the nanoparticle itself.

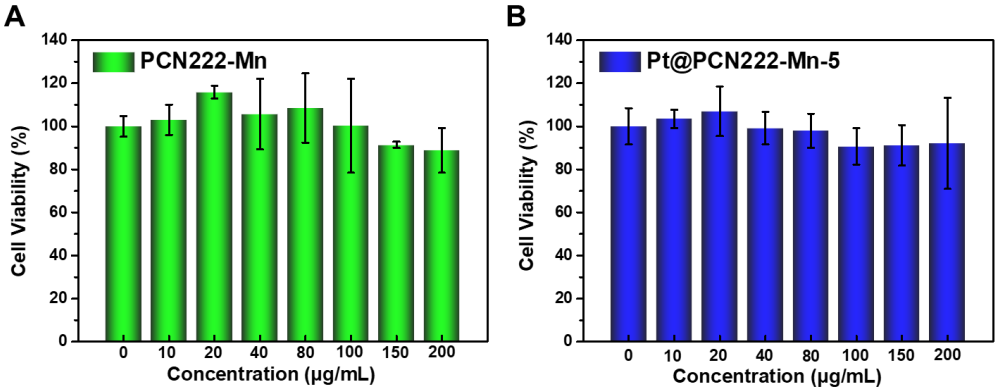

Figure S16. Viability of CT-26 cells upon treatment with different concentrations of (A) PCN222-Mn and (B) Pt@PCN222-Mn-5. Data are shown as mean ± SD (n = 5).

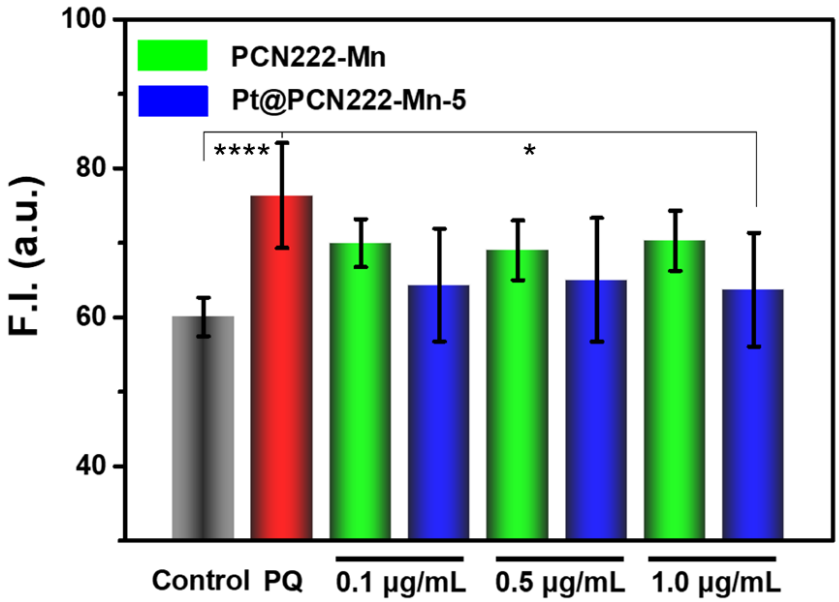

Figure S17. Fluorescence of DCFH-DA from CT-26 cells pre-treated with paraquat (PQ) (5 mM) for 3 hours following treatment with different concentrations of PCN222-Mn and Pt@PCN222-Mn-5. Data are shown as mean ± SD (n = 5). *P < 0.05, ****P < 0.001, *t*-test.

The ROS scavenging activity of PCN222-Mn and Pt@PCN222-Mn-5 was further evaluated by monitoring their activities against paraquat-induced intracellular ROS levels of CT-26 cells. As shown in Fig. S17, both PCN222-Mn and Pt@PCN222-Mn-5 showed ROS scavenging activities while Pt@PCN222-Mn-5 exhibited the better one.

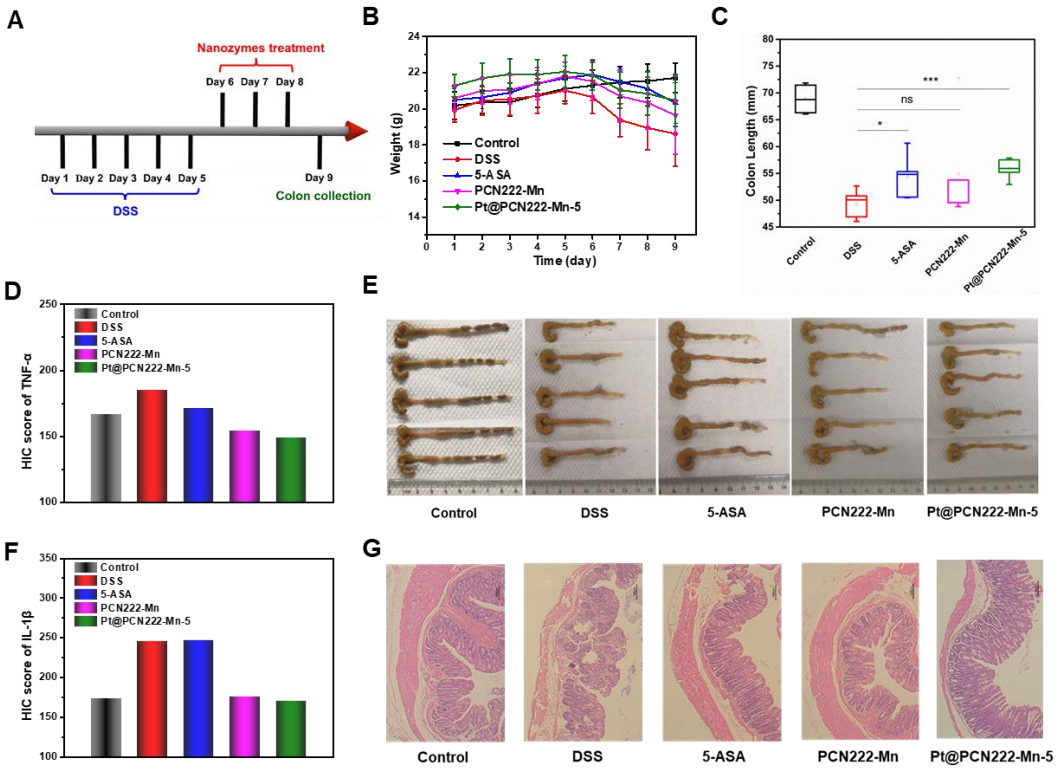

Figure S18. (A) Overall procedure of the animal experiment. (B) Daily body weight development for 9 days. (C) Colon lengths and (E) the corresponding images of the colons in indicated groups. Immunohistochemistry (IHC) scores of (D) TNF-α and (F) IL-1β in colon homogenates from indicated groups. (G) Hematoxylin and eosin stained colonic sections of mice from indicated groups on Day 9. Dose of 5-ASA, PCN222-Mn, and Pt@PCN222-Mn-5 were at 1 mg/kg. The data are shown as mean ± SD (n = 5). *P < 0.05, ***P < 0.005, ns = not significant, *t*-test.

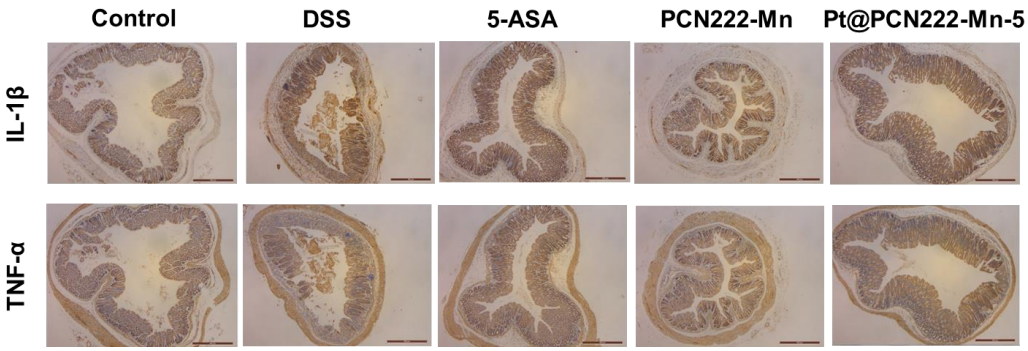

Figure S19. IHC images of colon tissues. Scale bar, 500 μm.

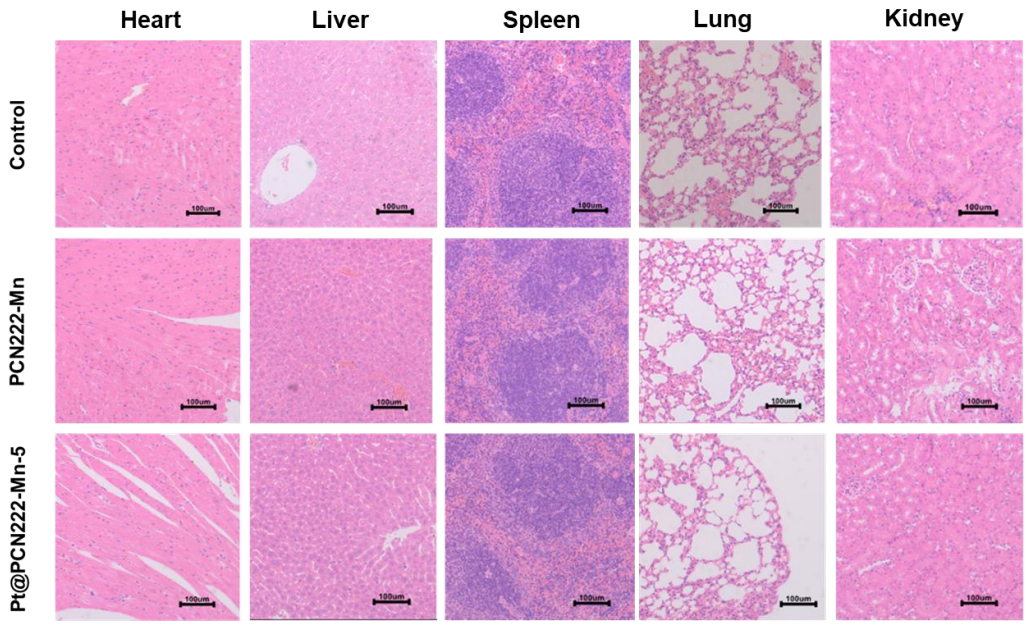

Figure S20. H&E stained histology sections of different tissues on Day 7 after injection with PCN222-Mn and Pt@PCN222-Mn-5 (1.0 mg/kg) for once. Scale bar, 100 μm.

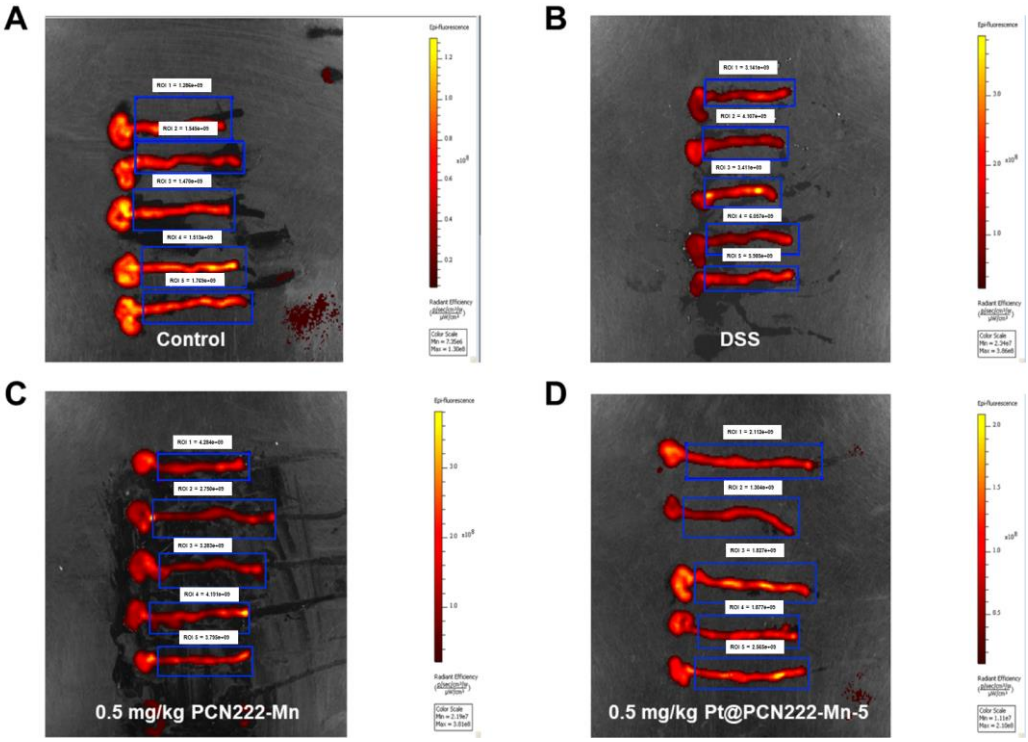

Figure S21. After the overall treatment procedure, on Day 10, the fluorescent imaging of colons in the groups of (A) Control, (B) DSS, (C) 0.5 mg/kg PCN222-Mn, and (D) 0.5 mg/kg Pt@PCN222-Mn-5 was performed by intraperitoneal injection of DCFH-DA. λ_{ex} = 465 nm, λ_{em} = 520 nm.

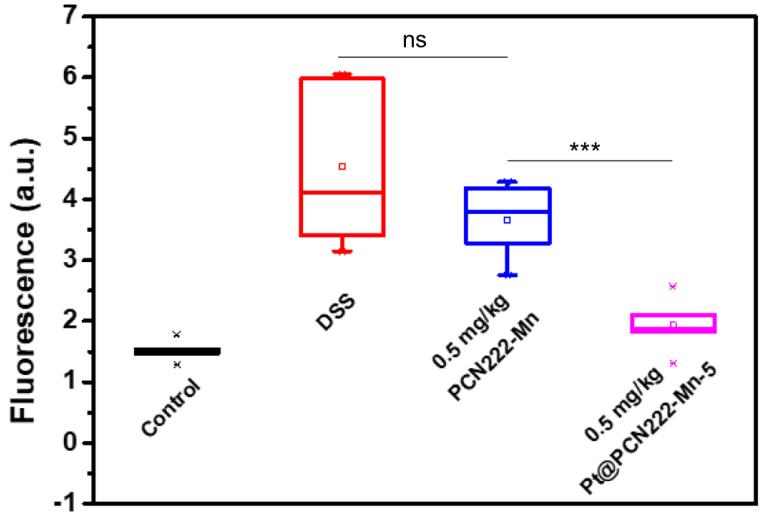

Figure S22. Fluorescent intensity of DCFH-DA in colon tissue of mice from indicated groups. The data are shown as mean ± SD (n = 5). ***P < 0.005, ns = not significant, *t*-test.

Table S1. BET surface area and porosity data.

Nanozymes	S_{BET} (m^2g^{-1})	Total pore volume (cm^3g^{-1})	Average pore diameter (nm)
PCN222-Mn	465.06	0.92	7.94
Pt@PCN222-Mn-5	572.23	0.77	5.39

Table S2. Zr content in typical tissues of mice measured using ICP-AES.[a]

Tissues	Control	Day 1	Day 7
Liver	ND	0.565 ± 0.076	0.294 ± 0.020
Spleen	ND	ND	ND
Kidney	ND	ND	ND

[a]The tissues of mice were collected on days 1 and 7 after intraperitoneal injection of Pt@PCN-222 at dose of 1 mg/kg. The tissues were dissolved in aqua regia at 120 °C for 4 h. The content of Pt and Zr in the sample were determined with inductively coupled plasma atomic emission spectrometer (ICP-AES). (unit: μg/g tissue) ND = Not detected. Data are means ± s.d. (n = 3).

To better study the fate of these nanoparticles, we have measured the content of Pt and Zr in different tissues by using ICP-AES instead of bio-TEM, the latter was not available for us currently. As shown in Table S2, the content of Pt in each sample was at quite low level, lower than the detection limit of the ICP-AES (0.1 ppb). The same situation was also observed for the content of Zr in spleens and kidneys of each group, as well as Zr in the liver of control group. Therefore, the intraperitoneally administrated Pt@PCN-222-Mn-5 was mainly metabolized in liver rather than spleen or kidney, which was beneficial to lowering organ accumulation and systemic toxicity.